Taylor & Francis
Taylor & Francis Group

🔓 OPEN ACCESS | Check for updates

Decomposition of Sulfide Phases and Subsequent Matte Collection in the Black Top of a Platinum Group Metal Smelter

Oscar Rivera Li Kao [ORCID] and Andrie Garbers-Craig [ORCID]

Centre for Pyrometallurgy, Department of Materials Science and Metallurgical Engineering, University of Pretoria, Hatfield, South Africa

ABSTRACT

This study explored, on a laboratory scale, how matte separates from the gangue in the black top of a PGM smelter. Two PGM concentrates, one with high sulfide content (17.3 mass%, Platreef concentrate) and the other with low sulfide content (1.3 mass%, UG-2 concentrate), were studied in the temperature range of 800°C to 1480°C, which is the temperature gradient across the black top. The results showed that effective matte separation occurs at temperatures when the matte is completely molten, and a substantial amount of liquid silicate phase has formed. The main matte separation mechanism is the coalescence of sulfide prills and their gravitational settling through the continuous path created by the liquid silicate phase. Complete matte separation occurs at lower temperatures in Platreef concentrate (1400°C in Platreef concentrate vs. 1480°C in UG-2 concentrate), due to the higher concentration of liquid silicate phase of lower viscosity, as well as the higher amount of sulfide minerals in this concentrate. PGMs already dissolve and collect in a nickel-iron-based alloy associated with the matte at temperatures as low as 900°C.

Introduction

Ores from the Bushveld Complex (South Africa) and the Great Dyke (Zimbabwe) are exploited in Southern Africa to extract their platinum-group metals (PGMs). The ore types in South Africa include the UG–2 (Upper Group Chromitite Reef No. 2) and Platreef reefs, while the most important PGM-mineralized zones of the Great Dyke in Zimbabwe are associated with the six-metal-enriched (Pt, Pd, Rh, Au, Cu and Ni) Main Sulfide Zone (Cawthorn 2006; Charlier et al. 2015). The Merensky reef in South Africa, which contained between 2 and 4 volume% base-metal sulfide (BMS) minerals (Charlier et al. 2015) and 3–9 g/t PGMs (Engelbrecht 2012; Schouwstra, Kinloch, and Lee 2000), has been mostly depleted (Cramer 2001). As a consequence, mainly UG–2 and Platreef ores are currently processed in South Africa. Ore from the UG–2 reef contains 4–7 g/t PGMs, with platinum the most abundant (Engelbrecht 2012; McLaren and De Villiers 1982; O'Connor and Alexandrova 2021). The UG–2 ore has a low concentration of base metal sulfides, containing the main sulfide minerals pentlandite, $(Fe,Ni)_9S_8$, (~0.9 mass %) and chalcopyrite, $CuFeS_2$, (~0.4 mass %). Platreef ore contains 2–5 g/t PGMs (O'Connor and Alexandrova 2021), but a higher concentration of sulfides than the UG-2 ore (1–10 volume %). Ore from the Great Dyke contains approximately 3–4 volume % sulfide minerals, which occur as a sulfide assemblage consisting of pyrrhotite, $Fe_{(1-x)}S$, pentlandite, chalcopyrite and subordinate pyrite (Mberi, Mguni, and Ntuli 2018; Stribrny et al. 2000). Oberthür (2011) reported that the ore grades of current PGM mines range from 1.16 g/t (Pt+Pd) in the Musengezi subchamber (subeconomic), up to 4.8 g/t (Pt+Pd+Rh+Au) in the Hartley platinum mine.

The PGM-containing ores are concentrated by two or three stages of milling and flotation (Engelbrecht 2012). The produced PGM concentrates have different sulfur contents: UG–2 concentrate contains 1–5 mass% S, Platreef reef concentrate 8–13 mass % S, while Unki concentrate from the Great Dyke in Zimbabwe contains 6–7 mass% S (Table 1). PGM concentrations in the concentrate vary between 80 and 600 g/t (Ramonotsi 2011). The produced PGM-containing concentrates are dried and smelted to separate the gangue (in the form of a SiO_2–MgO–FeO–based slag) from the PGM-containing Fe–Ni–Cu–Co-based matte. During the smelting process, a layer of unsmelted concentrate (called the 'black top' (BT)) floats on top of the molten slag bath. This layer limits the thermal radiation from the molten bath, thereby protecting the refractory materials in the upper parts of the furnace (Jones 2005; Rivera Li Kao and Garbers-Craig 2022). The slag produced from UG–2 concentrate contains higher concentrations of Cr_2O_3, MgO and SiO_2 compared to Platreef concentrate (Table 1). These higher concentrations of chromium oxide (Cr_2O_3) and magnesium oxide (MgO) in the UG–2 concentrates increase the liquidus temperature of the slag, while the high silica content increases the viscosity of the slag. Sulfide phases start to decompose in the BT and begin to collect as matte as soon as a continuous liquid silicate phase forms in the sintered concentrate through which the matte droplets can descend (Jones 2005; Rivera Li Kao and Garbers-Craig 2022).

Table 1. Chemical compositions of the UG–2, platreef and unki concentrates (mass %) (Adams, Liddell, and Holohan 2011; Barnes and Newall 2006; Buchspies et al. 2017; Crundwell et al. 2011; Eksteen, Van Beek, and Bezuidenhout 2011; Gwimbi 2017; Jones and Kotzé 2004; Liddell 2009; Mabiza 2006; Muzawazi and Petersen 2015; Mwase, Petersen, and Eksteen 2012; Rivera Li Kao and Garbers-Craig 2022).

	UG-2	Platreef	Unki
SiO_2	40.4–49.6	34.7–42.4	44.8
MgO	17.7–24.7	13.3–17.2	21.0–24.0
Al_2O_3	2.9–5.0	2.6–7.0	1.4
CaO	2.2–3.0	2.9–5.6	2.2
Cr_2O_3	1.1–5.0	0.1–0.4	0.29
Fe*	8.3–15.5	14.1–18.4	13.0–15.2
Ni	0.4–2.8	1.5–4.1	2.0–3.7
Cu	0.2–1.6	1.2–2.3	1.5–2.7
Co**	0.1	0.1	0.12
S	0.9–5.3	8.0–12.8	6.0–7.2

*: Total iron expressed as Fe; Fe partitions between the sulfide, silicate and oxide phases.
**: Maximum values found in the literature.

PGMs occur in nature as alloys, sulfides, sulfarsenides, arsenides, antimonides, bismuthides and tellurides (Mwase, Petersen, and Eksteen 2012), with the sulfides, arsenides and tellurides being the most common (Vermaak 2005). The PGMs can also occur in very low concentrations in other minerals in the form of submicroscopic particles or in solid solution (with base metal sulfides being the major repository of PGMs), making locating and identifying these PGMs very difficult (Oberthür, Weiser, and Kojonen 2002; Vermaak 2005). Pentlandite is the main Pd carrier, while pyrrhotite, pyrite and chalcopyrite contain PGMs in very low concentrations (Vermaak 2005). The mineralogy and distribution of the PGMs are, however, specific to the host ore body. UG–2 ores contain more PGM sulfides, such as braggite ((Pt,Pd)S), cooperate (PtS), malanite ($CuPt_2S_4$) and laurite (($Ru,Os)S_2$) (McLaren and De Villiers 1982; Vermaak 2005), with Pt-Pd-tellurides being dominant in the Platreef ore, although arsenides, alloys and sulfides are also present (O'Connor and Alexandrova 2021; Wilson and Anhaeusser 1998). In the Platreef ore, the platinum group minerals occur in association with base metal sulfides (enclosed in or on grain boundaries) but also have a high association with silicate minerals in some areas (Schouwstra, Kinloch, and Lee 2000). According to Wilson and Anhaeusser (1998) the tellurides and arsenides are mostly embedded in the silicate gangue. In UG-2, the PGM-containing minerals occur in association with the base metal sulfides and silicates, with only laurite (($Ru,Os)S_2$) having a preferred association with the chromite grains (Schouwstra, Kinloch, and Lee 2000). The average size of PGM-containing minerals in the UG–2 is approximately 12 μm and rarely exceeds 30 μm and is significantly smaller than those found in the Platreef ore (40–200 μm) (Engelbrecht 2012; Schouwstra, Kinloch, and Lee 2000).

Due to the low concentrations of sulfides in PGM concentrates, autothermal smelting (as used in the copper industry where the concentrates contain 20–30 mass% S) is not feasible (Bacedoni, Moreno-Ventas, and Ríos 2020). The low sulfides content of the UG–2 reef (compared to Platreef, Merensky and Great Dyke concentrates) requires blending in order to facilitate matte collection during smelting. It has been reported that a matte-fall of at least 15% is required for good collection and high recovery of PGMs (Nell 2004). Blending also controls slag liquidus temperatures (and therefore also matte superheat) and slag viscosities (which influences entrainment and PGM losses to the slag) (Shaw et al. 2013).

The primary production of PGMs entails two main pyrometallurgical operations in which matte is produced: primary smelting of the PGMs concentrates to produce an iron-rich Fe-Ni-Cu-Co-based matte that contains the PGMs, and the subsequent converting of the furnace matte to produce a PGM-enriched Ni-Cu-Co-based matte. Smelting of PGM concentrates is done in electric furnaces (rectangular six-in-line electrode or circular three-electrode furnaces), while converting of the furnace matte (to remove some of the sulfur and most of the iron) is done in either Peirce Smith converters (PSC) or in the Anglo Platinum Converting Process (ACP) converter, which uses an adapted Sirosmelt process (Jones 2004; Nelson et al. 2018).

This study investigated the behavior of sulfides in UG–2 and Platreef concentrate as they descend through the BT, including the mechanisms that control matte collection and PGM recovery in the BT. This was done by performing isothermal laboratory-scale experiments.

Background

Decomposition and melting of sulfide minerals

The main sulfide minerals in PGM concentrate, pentlandite, chalcopyrite and pyrite, decompose in an inert atmosphere at temperatures ranging from 500 to 610°C. Upon decomposition, these minerals form solid sulfides $(Fe,Ni)_{1-x}S$, $Ni_{3\pm x}S_2$ (heazlewoodite), Cu_2S (chalcocite), Cu_5FeS_4 (bornite), $Fe_{1-x}S$ and FeS (troilite), according to the reactions given in Table 2. Both chalcopyrite and pyrite decompose with an accompanying release of sulfur gas. Prasad and Pandey (1999) reported that chalcopyrite decomposes into chalcocite, troilite and sulfur, while Gaballah et al. (1994) reported that chalcopyrite decomposition occurs in two stages, forming cubanite ($CuFe_2S_3$), chalcocite and sulfur in the first stage. After this, cubanite and chalcocite react to form bornite and troilite, with a further

Table 2. Decomposition reactions of main sulfides found in PGM concentrate (*Kullerud 1963; #Prasad and Pandey 1999; ##Gaballah et al. 1994; ΔXu et al. 2019).

Reaction	Temperature (°C)
$Fe_{4.5}Ni_{4.5}S_{8(s)} \rightarrow (Fe, Ni)_{1-x}S_{(s)} + Ni_{3\pm x}S_{2(s)}$	610 ± 2*
$2CuFeS_{2(s)} \rightarrow Cu_2S_{(s)} + 2FeS_{(s)} + S°$	524#
$4CuFeS_{2(s)} \rightarrow 2CuFe_2S_{3(s)} + Cu_2S_{(s)} + S°$	500##
$2CuFe_2S_{3(s)} + Cu_2S_{(s)} \rightarrow 0.8Cu_5FeS_{4(s)} + 3.2FeS_{(s)} + 0.6S°$	
$(1-x)FeS_{2(s)} \rightarrow Fe_{1-x}S_{(s)} + \frac{(1-2x)}{2}S_{2(g)}$	$500–600^\Delta$

Table 3. Melting points of main sulfides found in PGM concentrate (#Madelung, Rössler, and Schulz 2000; ΔΔMineralogical Society of America 1974; ΔNieroda et al. 2020; ##Sugaki and Kitakaze 1998; **Ulbrich and Campos 2020; *Waldner and Pelton 2005).

Mineral compound	Formula	Temperature (°C)
Pyrite	FeS_2	743*
Heazlewoodite	Ni_3S_2	790**
Chalcopyrite	$CuFeS_2$	847; 877#
Pentlandite	$Fe_{4.5}Ni_{4.5}S_8$	865 ± 3##
Chalcocite	Cu_2S	1130^Δ
Pyrrhotite	Fe_7S_8	$1190^{\Delta\Delta}$

*: Decomposes into pyrrhotite and liquid sulfur, Waldner and Pelton (2005).
**: Bulk Ni_3S_2 (nanocrystallites of Ni_3S_2 are reported to have a melting point of 660°C, Ulbrich and Campos 2020).
#: Reported temperatures, Madelung, Rössler, and Schulz (2000).
##: Breaks down into monosulfide solid solution and liquid, Sugaki and Kitakaze (1998).
Δ: Melting point of pure Cu_2S, Nieroda et al. (2020).
ΔΔ: Maximum melting temperature, Mineralogical Society of America (1974).

Table 4. Liquidus temperature ranges of matte and slag of pure and blended UG–2, Platreef and Merensky PGM concentrates (°C) (Eksteen 2011; Eksteen, Van Beek, and Bezuidenhout 2011; Jones 2005; Rivera Li Kao and Garbers-Craig 2020; Shaw et al. 2013.).

Matte	Slag
850–875	1350–1680

release of sulfur. Gaballah et al. (1994) did not observe chalcocite as a decomposition product. The decomposition reactions of the sulfides occur at temperatures lower than those at which the first gangue mineral (talc) starts to decompose, i.e. 800°C (Rivera Li Kao and Garbers-Craig 2022). The pure sulfides melt at temperatures ranging from 743 to 1190°C (Table 3), while the liquidus temperature of the matte has been reported to be below 900°C (Table 4). The liquidus temperature of the matte is therefore lower than the solidus temperature of the gangue of the concentrates, as predicted by FactSage (1100°C for Platreef and 1250°C for UG–2, Rivera Li Kao and Garbers-Craig 2022), which implies that the matte will be fully molten before melting of the silicate gangue matrix and liquid-state sintering start. The higher solidus temperatures exhibited by the gangue constituents also imply higher liquidus temperatures associated with the slag (Table 4) and therefore high superheat associated with the matte (Eksteen 2011; Eksteen, Van Beek, and Bezuidenhout 2011; Jones 2005; Rivera Li Kao & Garbers-Craig 2022; Shaw et al. 2013).

Matte–slag separation

Conventional matte–slag separation is a liquid–liquid separation process in which the matte droplets within the slag bath coalesce, increase in size and then settle through the slag into the matte phase due to density differences (Guntoro et al. 2018). Guntoro et al. (2018) studied the reaction sequences and matte–slag separation at 1300°C in air and argon atmospheres, for a mixture of synthetic fayalitic slag and chalcopyrite concentrate. They observed (under both atmospheres) that matte coagulation occurs only after a substantial amount of liquid slag is formed. Similar observations were reported by Fagerlund and Jalkanen (2001), for a copper sulfide matte settling through liquid wollastonite slag.

When the concentrate moves down through the BT (which has a temperature gradient from 800°C at the freeboard–BT interface, up to 1500°C at the BT–slag interface) and reaches the solidus temperature of the gangue (~1200 °C), sintering of the concentrate bed starts to take place. At this point, several matte droplets may become entrained in the closed pores generated by the sintering process. At higher temperatures, the generation of a liquid silicate phase (LP) in the gangue promotes matte drainage through LP channels that form in the silicate matrix. The matte subsequently separates from the gangue minerals at sub-liquidus temperatures of the gangue (Rivera Li Kao and Garbers-Craig 2022).

In a theoretical study on South African PGM matte drainage through a concentrate bed, Eksteen (2011) developed mathematical models for matte drainage that considered the mean particle size and mineralogy of the PGM concentrate. Eksteen (2011) highlighted the importance of the permeability of the BT, as the sintering of the black top and the subsequent accumulation of matte in the concentrate bed above the slag bath can lead to several problems, including (1) hindering the escape of gases (CO, CO_2, H_2O, S_2 and volatile metal halides), which then might move sideways, recondense on the copper

coolers in the sidewalls of the furnace, and cause chlorine-induced sulfide attack of the copper coolers (Shaw et al. 2013); (2) the need to increase the ingress airflow to reduce freeboard temperatures, resulting in higher electrode consumption; (3) uneven heat transfer in the matte accumulation zones; and (4) changes in the physical properties of the BT. These factors can cause significant matte superheat, with matte temperatures above 1500°C. If the matte temperature exceeds the liquidus temperature of the freeze lining, the matte can potentially destroy the freeze lining. This destruction can then lead to catastrophic failures in the refractory and copper coolers within the furnace.

Materials and methods

Raw materials

Experiments were conducted using two PGM concentrates: a concentrate with a low-sulfide concentration (UG–2, 1.32 mass%) and a concentrate with a high-sulfide concentration (Platreef, 17.33 mass%). A significantly higher matte fall (percentage of the mass of matte collected per tonne of concentrate) can, therefore, be expected from the Platreef concentrate. The chemical and mineralogical compositions of these concentrates are reported elsewhere (Rivera Li Kao and Garbers-Craig 2022).

Experimental setup

Laboratory-scale experiments simulated the thermal gradient across the BT of an industrial smelter. UG–2 and Platreef concentrates were contained in magnesia (MgO) and silica (SiO_2) crucibles, respectively. In order to prevent the escape of sulfur-containing gases from the concentrate on heating, the experiments were carried out in steel capsules (Figure 1), which were purged with argon before being sealed. The steel capsules were heated in an argon-controlled atmosphere in a muffle furnace. The heating process started from room temperature and gradually reached the desired temperature (800/900/1000/1100/1200/1300/1400 and 1480°C) at a heating rate of 10°C min^{-1}. The samples were kept isothermally at the target temperature for 2 h. After reaction, the capsules were cooled down inside the furnace. The study also investigated the impact of a high sulfur pressure inside the sealed capsules of Platreef concentrate on phase relations and matte collection. This was achieved by comparing the matte drainage and phase relations in sealed capsules with those in capsules that had a 1 mm diameter hole in their lids. The hole allowed the release of excess pressure from the system (Figure 1). Quench tests were also conducted on the Platreef concentrate in sealed capsules at temperatures of 1400 and 1480°C, in order to determine how cooling rates impact matte collection.

Characterization techniques

The chemical and mineralogical compositions of the bulk concentrates were determined using inductively coupled plasma–optical emission spectroscopy (ICP–OES) and a LECO sulfur analyzer (Rivera Li Kao and Garbers-Craig 2022). The crystalline phases were identified with X-ray diffraction (XRD), using a PANalytical X'Pert Pro powder diffractometer with Co Kα radiation (λ = 1.789 Å), employing the ICSD (Inorganic Crystal Structure Database) and X'Pert Highscore Plus software. The quantification of crystalline phases was obtained by Rietveld refinement of the XRD patterns.

The metallographic preparation of the raw and fired concentrates was carried out by embedding the samples in AKASEL epoxy resin. The resin was cured at 70°C for 24 h and the mounted samples were subsequently ground and polished using silicon carbide paper (200# to 1200#) and diamond suspensions of 9.0, 6.0 and 1.0 μm, respectively.

An Olympus BX51–M optical microscope was used for analyzing the distribution of sulfide minerals and matte in the concentrates and fired samples. The images were processed using a Fiji image processing package (Schindelin et al. 2012), to investigate the number of particles, their average size and circularity, and the area covered by sulfides or matte. The acquired images have resolutions of 2080 × 1544 pixels, with the magnification varying (50× and 100×) depending on the size of the analyzed sulfide particles or matte droplets.

The chemical compositions and morphologies of the observed phases were determined by using a Jeol JSM – IT300LV scanning electron microscope (SEM) coupled with an Oxford X-Max 50 Energy-Dispersive X-ray Spectrometer (EDS). The obtained EDS spectra were processed and refined individually after acquisition using standardless EDS analysis. The samples were coated using a Quantum carbon coater.

Figure 1. Schematic views of the sealed capsule system (a) and the capsule with a drilled hole (b).

Thermochemical predictions

The solidus and liquidus temperatures of the sulfide systems were predicted (under equilibrium conditions) using FactSage® 7.3 (Bale et al. 2016). The equilibrium calculations were performed in the Equilib module, using the FactPS and FToxid database.
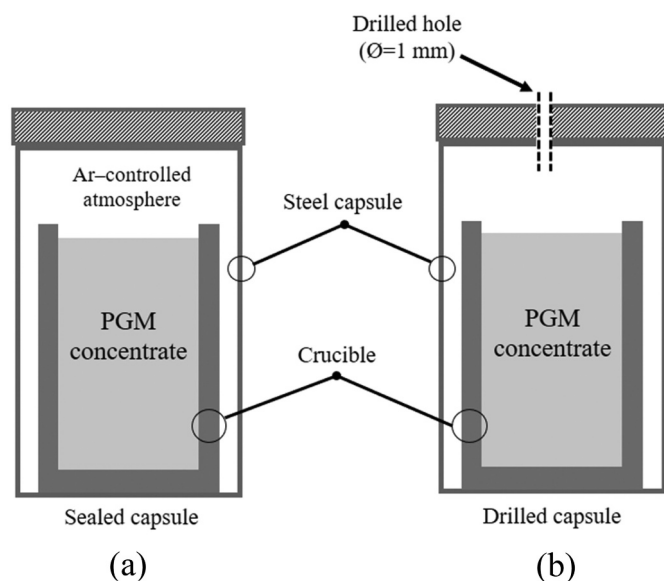
Since the samples were all reacted in closed steel capsules, it was assumed that the steel capsules would control both the oxygen and sulfur partial pressures in the capsules through the iron–wüstite (Fe/FeO) and iron–troilite (Fe/FeS) equilibria, respectively. The sulfur partial pressure was obtained from the Predom module (Fe–S–O system), for all the selected temperatures and their respective oxygen partial pressures. The oxygen partial pressures used in the FactSage calculations therefore ranged from 10^{-18} (800°C) to 10^{-9} (1480°C) bar, while the sulfur partial pressures ranged from 10^{-9} (800°C) to $10^{-3.5}$ (1480°C) bar. The production of sulfur gas was evidenced in the detection of sulfur-containing compounds in the walls of the steel capsules.

Results

Characterization of the sulfide phases in the PGM concentrates

The normalized sulfide mineral contents in UG–2 and Platreef concentrates obtained from the Rietveld refinement of the XRD patterns are shown in Table 5. UG–2 concentrate mainly contains a mixture of pentlandite and chalcopyrite, approximately in a 2:1 mass ratio, while the Platreef concentrate consists of pentlandite, chalcopyrite and pyrite in a 2.4 : 2.2 : 1 mass ratio. Pyrite occurs in very low concentrations in the UG-2 concentrate and, as a result, could only be detected through SEM analysis.

The chemical compositions of the different sulfide minerals detected by XRD in the as-received PGM concentrates were determined through individual SEM–EDS analyses of each reported phase. The average EDS compositions (from 100 analyses) for major and trace elements in both concentrates are given in Table 6, while the calculated stoichiometries for these average EDS analyses are given in Table 7. Pentlandite in UG-2 concentrate contains lower amounts of nickel and has a lower cation/sulfur atomic ratio (i.e. is less stoichiometric) than in Platreef concentrate. The stoichiometry of chalcopyrite is similar in the UG-2 and Platreef concentrates, while pyrite contains slightly more copper in the UG-2 concentrate than in the Platreef concentrate.

The total chemical compositions of the sulfide mixtures were calculated using the XRD (Table 5) and SEM–EDS data (Table 6). These values (Table 8) were used as the basis for the thermochemical calculations in FactSage®. The most significant differences between the two types of concentrates are the higher nickel and cobalt content in UG–2 concentrate and its lower sulfur, iron and copper content compared to the Platreef concentrate (Table 8). The UG-2 concentrate has a higher bulk metal/sulfur atomic ratio than the Platreef concentrate (0.99 vs. 0.88, respectively), while the $(Ni + Cu)/\Sigma$metal atomic ratios of the two concentrates are very similar (0.49 vs. 0.42 for UG-2 and Platreef, respectively). A higher bulk metal/sulfur ratio corresponds to a lower solidus temperature of the concentrate (Ballhaus, Tredoux, and Späth 2001). Chromium was only detected in UG–2 concentrate (0.03 mass %).

Morphologies of the sulfide phases in the as-received PGM concentrates

The backscattered electron images (BEIs) of the as-received PGM concentrates are presented in Figure 2(a,b). Sulfides in these concentrates are present as monophase sulfides as well as

Table 5. Sulfides content (normalized) in UG–2 and platreef PGM concentrates.

	Sulfide components (mass %)		
Concentrate	Pentlandite	Chalcopyrite	Pyrite
UG–2	67.4	32.6	0.0
Platreef	43.6	38.5	17.9

Table 6. Average SEM–EDS analyses of the sulfide phases in the PGM concentrates (mass %).

	S	Fe	Ni	Co	Cu	Cr
Pentlandite						
UG–2	35.28 ± 0.76	30.27 ± 2.91	33.17 ± 3.28	1.12 ± 1.00	0.14 ± 0.75	0.01 ± 0.06
Platreef	34.20 ± 0.39	29.23 ± 1.61	35.66 ± 1.58	0.91 ± 0.29	–	–
Chalcopyrite						
UG–2	37.45 ± 0.91	30.04 ± 0.38	–	0.04 ± 0.07	32.35 ± 0.71	0.12 ± 0.19
Platreef	36.39 ± 0.31	30.80 ± 1.02	0.06 ± 0.26	0.11 ± 0.12	32.63 ± 1.24	–
Pyrite						
UG–2	53.90 ± 0.66	43.79 ± 1.36	–	0.89 ± 0.00	1.43 ± 2.02	–
Platreef	54.40 ± 0.56	44.55 ± 0.79	0.21 ± 0.48	0.62 ± 0.56	0.22 ± 0.73	–

Table 7. Stoichiometries of the different sulfide phases found in the UG-2 and platreef PGM concentrates.

	Stoichiometry of sulfide phase		
	Pentlandite	Chalcopyrite	Pyrite
UG–2	$[Ni_{4.11}Fe_{3.94}Co_{0.14}Cu_{0.02}]_{\Sigma=8.21} S_8$	$[Cu_{0.87}Fe_{0.92}]_{\Sigma=1.79} S_2$	$[Fe_{0.93}Cu_{0.03}Co_{0.02}]_{\Sigma=0.98} S_2$
Platreef	$[Ni_{4.56}Fe_{3.93}Co_{0.12}]_{\Sigma=8.61} S_8$	$[Cu_{0.90}Fe_{0.97}]_{\Sigma=1.87} S_2$	$[Fe_{0.94}Co_{0.01}]_{\Sigma=0.95} S_2$

Table 8. Calculated total chemical compositions of the sulfide mixtures in the UG–2 and platreef concentrates (mass %).

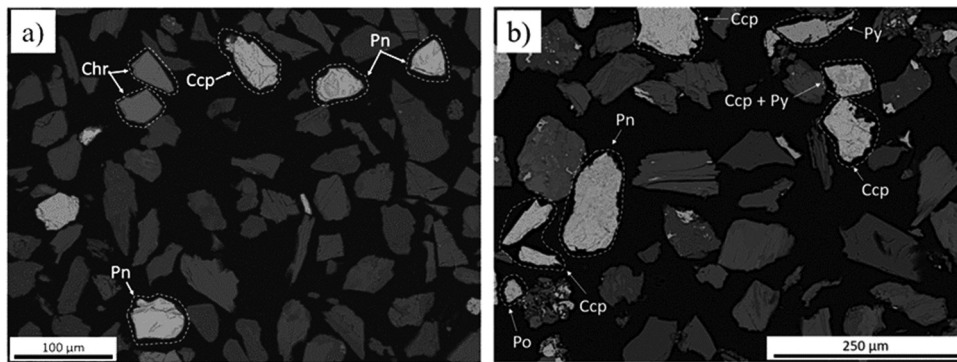| Concentrate	S	Fe	Ni	Cu	Co	Cr
UG–2	35.69	30.90	21.95	10.66	0.76	0.03
Platreef	38.72	33.35	14.68	12.72	0.53	0.00

Figure 2. BEI images of (a) UG–2 and (b) Platreef PGM concentrates (Ccp: chalcopyrite; Pn: pentlandite; Po: pyrrhotite; Chr: chromite; Py: pyrite).

sulfide assemblages consisting of pentlandite, pyrite and chalcopyrite. UG–2 sulfides exhibit a high degree of liberation, with a few microcracks in some of the particles, while Platreef sulfides exhibit a higher degree of association with gangue minerals and other sulfide phases. Generally, the sulfides exhibit sharp edges. The presence of chromite particles and the low concentration of sulfides in the UG–2 concentrate are apparent.

The low concentration of PGMs in the concentrates was evidenced by the detection of only one PGM mineral, michenerite ((Pd,Pt)BiTe), which was completely liberated. This palladium bismuth telluride was found exclusively in the Platreef concentrate, containing 22.0 wt% Pd, 42.5 wt% Bi, and 26.1 wt% Te.

FactSage® prediction of solidus and liquidus temperatures and liquid content of matte and silicates at different temperatures

FactSage predicts that the solidus temperature of UG–2 matte is lower (623°C) than that of Platreef matte (645°C). Both concentrates have estimated liquidus temperatures of 1000°C (Table 9), with a nickel–iron solid solution alloy phase which precipitates as primary phase on cooling. Despite the earlier onset of liquid matte formation in UG–2 concentrate, the amount of liquid matte which forms in Platreef concentrate is significantly higher and contributes more to the total liquid content in the black top (compare Figures 3 and 4).

Table 9. FactSage predicted solidus and liquidus temperatures for UG–2 and platreef matte and silicates.

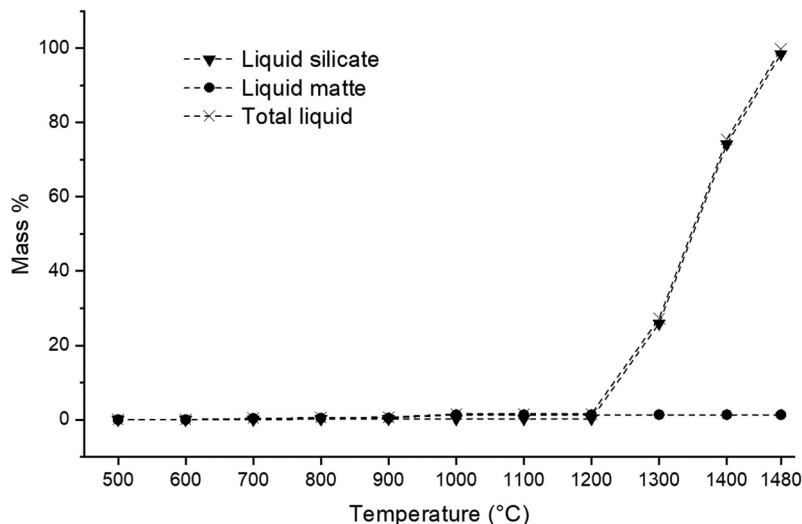| Concentrate	Solidus (°C)	Liquidus (°C)	Melting range (°C)	Primary phase
Matte:				
UG–2	623	1000	277	Nickel–iron solid solution alloy
Platreef	645	1000	355	Nickel–iron solid solution alloy
Silicates:				
UG–2	1250	1600	350	Spinel
Platreef	1100	1500	400	Protopyroxene

Figure 3. Mass% liquid matte, liquid silicate and total liquid in the UG-2 concentrate as a function of temperature (predicted by FactSage®).
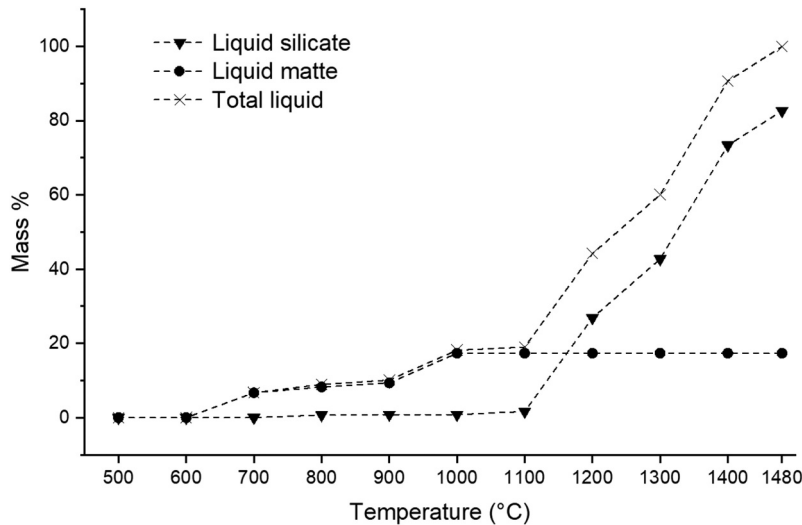
Figure 4. Mass% liquid matte, liquid silicate and total liquid in the platreef concentrate as a function of temperature (predicted by FactSage®).

Coalescence of the matte

The coalescence of the matte was studied by examining the changes in the number and average size of matte droplets (sulfide assemblages) as they descend through the BT. The analysis was performed only on the Platreef concentrate due to the challenge posed by the extremely low concentration of small-sized sulfide droplets in the UG–2 concentrate.

The number of matte droplets and their average size is plotted in Figure 5 as a function of temperature (299643 prills were analyzed in total). A simultaneous decrease in the number of sulfide particles and an increase in their average size were observed with increasing temperature. The increase in average size becomes noticeable at a firing temperature of 1200°C, which corresponds to the formation of approximately 26% liquid silicate and 17% liquid matte, totaling approximately 43% liquid.

At 1200°C and higher, the LP enabled matte prills to settle due to gravitational forces, increasing the likelihood of their collision and subsequent merging. This coalescence process led to a reduction in the quantity of matte prills and an increase in their average size as the temperature increased. Elevated temperatures, which result in higher

liquid concentrations, therefore create more favorable conditions for matte-gangue separation.

The large standard deviation in particle size at 1400°C can be attributed to the variation in size between the large coalesced droplets, which were attached to pores and were entrained in cavities, and the smaller droplets that were attached to pores and suspended in the liquid silicate phase. Conversely, the reduction in the particle size at 1480°C is due to the presence of large matte droplets, exceeding 1.27 mm in diameter, which were excluded from the calculation of the average particle size. The included droplets in the average particle size calculation were those entrained or suspended in the liquid silicate phase.

Phase and microstructural analysis of the sulfides and matte as a function of temperature

Crystallization sequence of the matte as predicted by FactSage®

Sulfide melts cannot be quenched to preserve their high-temperature phase relations; they invariably recrystallize, no matter the cooling rate (Ballhaus, Tredoux, and Späth 2001). The
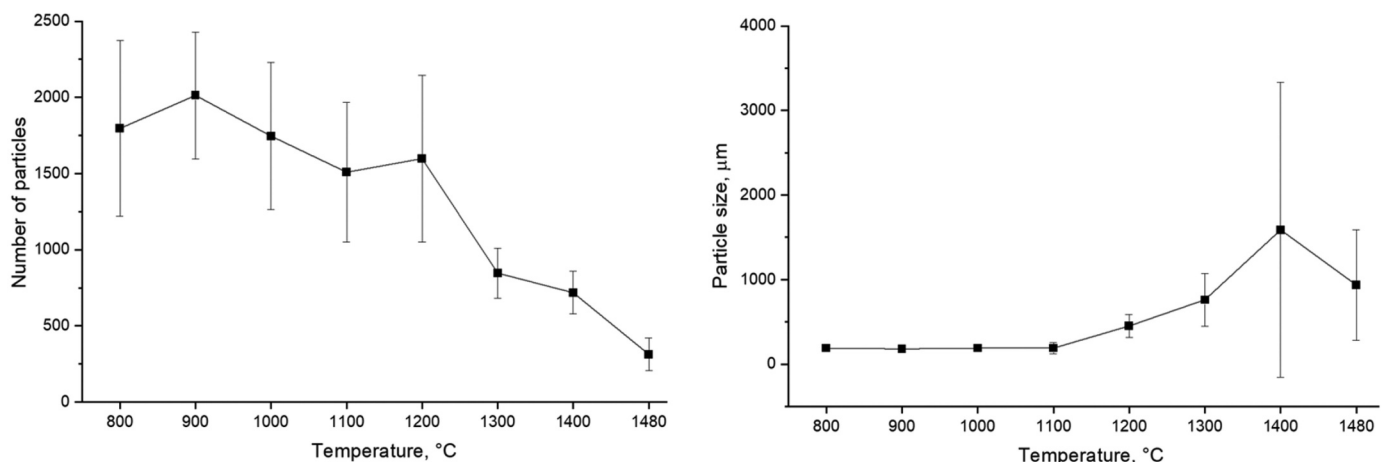

Figure 5. The evolution of matte prills (from platreef concentrate) in the slow-cooled experiments is depicted through: (a) the number of matte-forming assemblages and (b) average size of the matte-forming assemblages, both as a function of temperature.
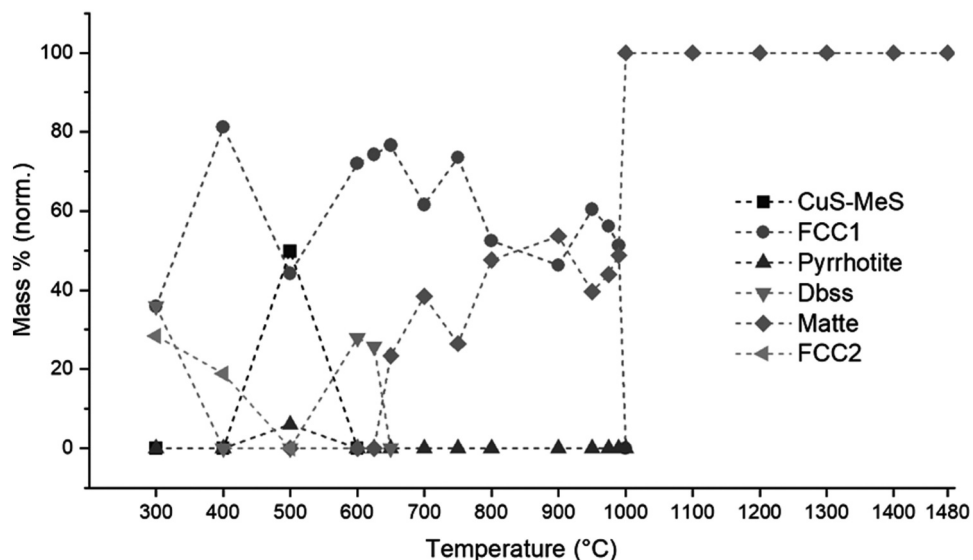
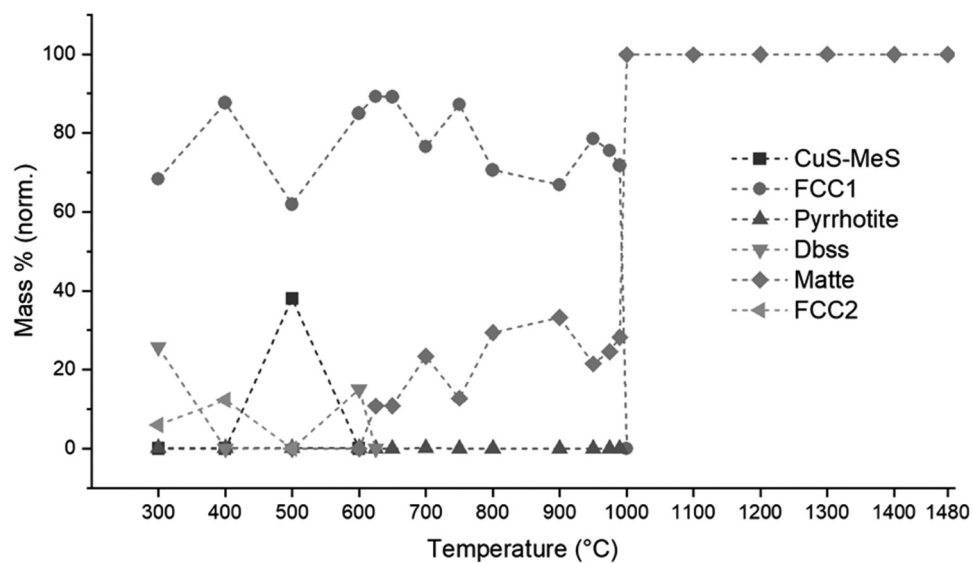Figure 6. Crystallization path of platreef matte.

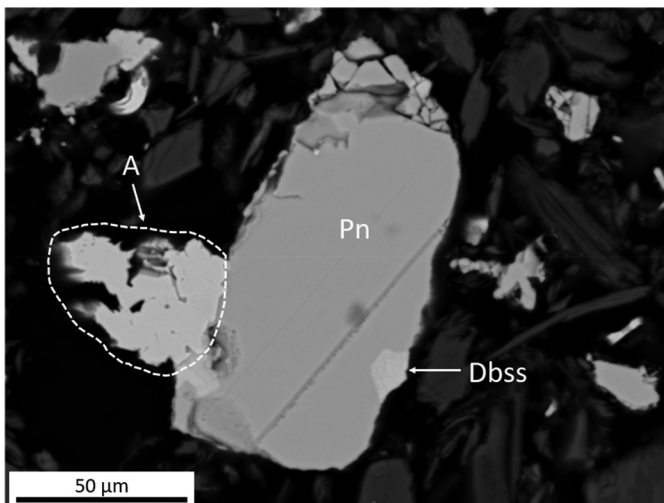

Figure 7. Crystallization path of UG–2 matte.

Figure 8. BEI of a sulfide assemblage from Platreef concentrate fired at 800°C, consisting of pentlandite (Pn), digenite–bornite solid solution (Dbss) and Ni-Fe solid solution alloy (A).

equilibrium crystallization paths of the Platreef and UG–2 mattes were, therefore, predicted using FactSage® (Figures 6 and 7), and these phases were compared to the phases observed in the furnace-cooled sulfide assemblages (Figures 8 and 9).

FactSage predicts that the phases that crystallize on cooling from the examined Platreef and UG–2 mattes are similar, although the proportions of these phases differ. A Ni–Fe solid solution alloy phase (FCC1) precipitates from both mattes as primary phase. FactSage® predicted a higher amount of Ni–Fe solid solution alloy in UG–2 matte compared to Platreef concentrate, due to the higher Ni concentration in the UG–2 matte (21.95 wt% Ni) compared to the Platreef matte (14.68 wt% Ni). At the solidus temperature, when the liquid matte is completely consumed, a digenite–bornite solid solution (dbss) phase (Cu_9S_5–Cu_5FeS_4), forms. The dbss phase in the Platreef has a stoichiometry of $Cu_{4.24}Fe_{1.88}S_4$ at 625°C and $Cu_{4.39}Fe_{1.81}S_4$ at 600°C, while in the UG-2 matte it has a stoichiometry of ($Cu_{4.34}Fe_{1.83}S_4$) at 600°C. The dbss phase
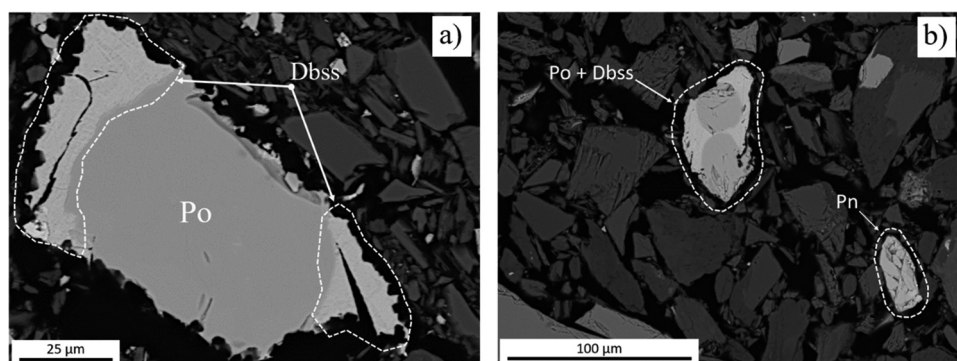
Figure 9. BEI of concentrates fired at 800°C revealing digenite–bornite solid solution (Dbss) – pyrrhotite (Po) assemblages present in both (a) Platreef concentrate and (b) UG–2 concentrate (Pn = pentlandite).

completely dissociates at 500°C, together with a partial consumption of the Ni–Fe solid solution phase, to form a CuS–MeS non-stoichiometric compound ($Fe_{1.34}Cu_{1.12}Ni_{0.20}S_2$) and pyrrhotite ($Fe_{0.98}Ni_{0.01}Co_{0.01}S$). A new copper-rich (>97 wt% Cu) solid solution alloy phase (FCC2) is formed at 400°C, while the dbss phase is completely consumed at this temperature. At 300°C, two solid solution alloy phases (FCC1 and FCC2) co-exist, while the dbss phase reforms due to the partial consumption of the FCC1 alloy phase.

Microstructural analysis

The microstructures of the matte-forming components obtained in the experiments are complex mixtures of sulfide phases (pentlandite (Pn), pyrrhotite (Po), digenite–bornite solid solution (dbss, C)) and Ni–Fe solid solution alloy phases. Only the most relevant microstructural changes are reported.

Samples heated at 800 and 900 °C. After being fired at 800°C, the sulfide particles present in both concentrates showed slight softening around their edges and displayed phases different from those found in the concentrates. The first newly formed phase is a Ni–Fe solid solution alloy, the growth of which was observed preferentially at the boundaries of the sulfide assemblages. The alloy crystals mainly consist of nickel and iron in an approximate atomic ratio of 2:1, falling within the compositional field of awaruite; i.e. between Ni_2Fe and Ni_3Fe (Anthony et al. 2005), with minor amounts of dissolved copper and cobalt. A sulfide assemblage in a Platreef sample, consisting mostly of pentlandite (Pn) to which an alloy (A) is attached, as well as a small amount of a dbss phase, is shown in Figure 8. The stoichiometry of the alloy is $Ni_{2.3}Fe$ and contains minor amounts of copper (1.6 at%) and cobalt (1.7 at%). The size of the observed dbss lamellae is too small for accurate compositional analyses (Figure 9(a)). However, an approximate stoichiometry of $Cu_{4.20}Fe_{1.22}S_4$ (based on four EDS analyses) was calculated for this phase, which is associated with pyrrhotite ($Fe_{0.92}S$). In the case of the UG–2, a dbss phase with $Cu_{4.19}Fe_{1.30}S_4$ stoichiometry, in association with pyrrhotite ($Fe_{0.93}S$, with 1.4 at% Cu and 0.4 at% Co), was observed (Figure 9(b)).

PGMs were detected in the alloy and sulfide phases of the sample fired at 900°C (Figure 10). The PGM particles in the sulfide matrix (bright spots, Figure 10) are enriched in palladium (30.6 at%), copper (22.3 at%) and lead (19.8 at%), while
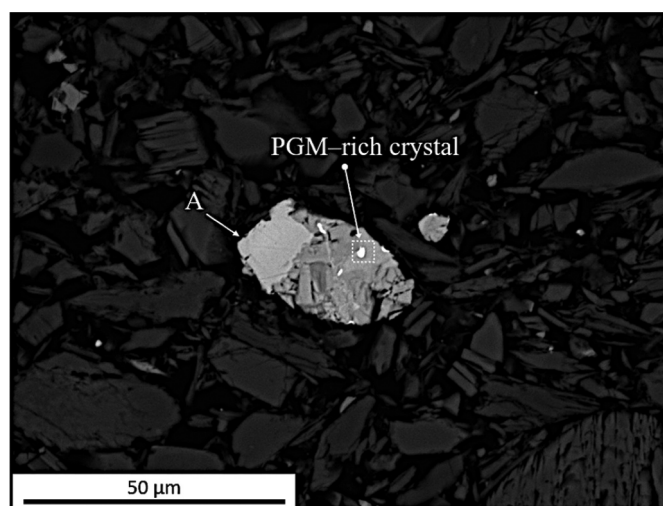

Figure 10. Sulfide particle in UG–2 concentrate fired at 900°C containing PGM-enriched crystals (bright spots) and a Ni-Fe-based alloy (A).

the alloy (phase A, Figure 10) has a stoichiometry of $Ni_{2.3}Fe$ and contains 3.3 at% Pd. Therefore, the collection of PGMs by the Ni–Fe-based alloy takes place at sub-liquidus temperatures of the matte.

Samples heated at 1000°C and 1100 °C. At a reaction temperature of 1000°C, the sulfide assemblages are more spherical and the alloy crystals bigger in size, suggesting that the sulfides were molten at this temperature. The sphericity of the sulfides increased as the firing temperature changed from 1000°C to 1100°C (compare Figure 11(a,b)). The alloy crystals in the UG–2, 1100°C sample are enriched in PGMs, although no PGMs could be detected in the Platreef samples. This is presumably due to the lower PGM content of the Platreef concentrate. At 1100°C, increased contact between the matte-forming assemblages and the gangue constituents of the concentrates was observed, especially in the Platreef concentrate.

Sample heated at 1200°C and 1300°C. The most significant difference that could be observed in the microstructures of both concentrates heated at 1200°C is the sintering of the concentrate bed (Rivera Li Kao and Garbers-Craig 2022). Conversely, it can be assumed that all the matte-forming
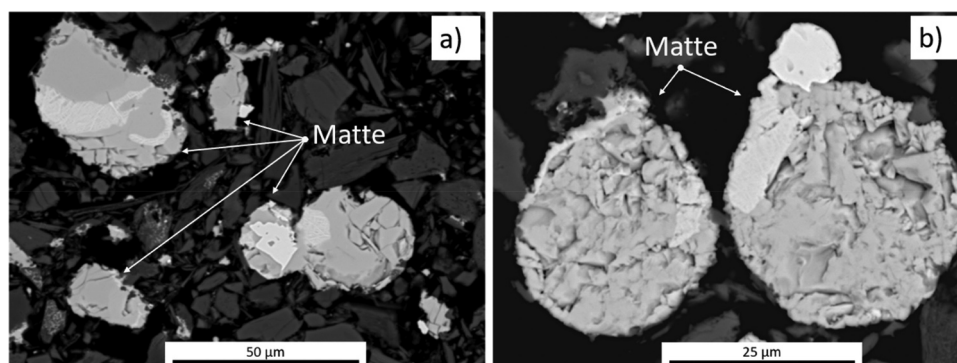
Figure 11. BEI of matte-forming assemblages (Platreef concentrate) exhibiting different degrees of sphericity after heating at (a) 1000°C and (b) 1100°C.
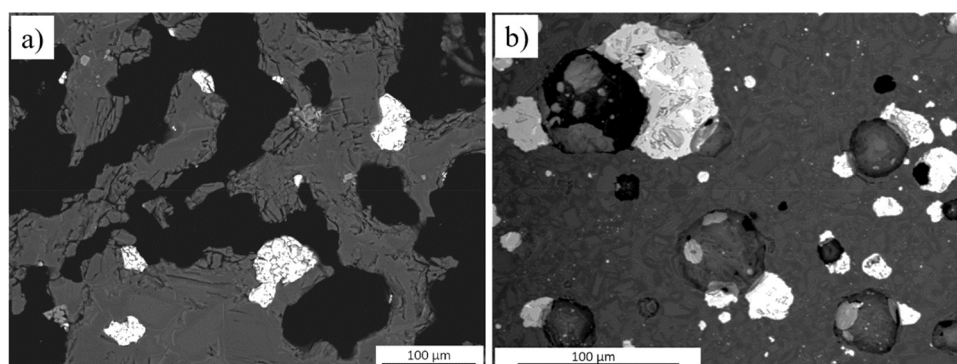

Figure 12. PGM concentrates fired at 1300°C (a) UG–2 concentrate (b) Platreef concentrate.

components were in the liquid state, given that the temperature had reached the highest melting point of the pure sulfide constituents, i.e. pyrrhotite, at 1190°C (Table 3).

After firing at 1300°C, the low amount of LP formed in the UG–2 concentrate matrix was still insufficient to facilitate the coalescence of matte prills. The sulfides remained mostly entrained within the cavities generated after sintering, thereby forcing the molten sulfides into irregular shapes (Figure 12(a)). However, the lower liquidus temperature of the gangue components in the Platreef concentrate allowed the formation of more LP in this concentrate at 1300°C, thereby reducing the overall porosity. Small matte droplets could be distinguished in the LP, with larger matte prills mainly associated with pores of irregular shapes (Figure 12(b)). The higher sulfide mineral content of the Platreef concentrate, compared to the UG–2 concentrate (17.3 vs. 1.3 mass%, Rivera Li Kao and Garbers-Craig 2022) and the predicted larger concentrations of liquid silicate in the Platreef concentrate (51.7% for Platreef concentrate and 26.2% for UG–2) promoted the partial separation of matte from gangue at this temperature.

Samples heated at 1400°C and 1480°C (slow-cooled, sealed capsules). Effective matte-gangue separation could only be observed in Platreef concentrate, due to the high amount of total liquid (liquid silicate + liquid matte) that formed at 1400°C (~91%, Figure 4) (Figure 13). The settling of matte prills through the liquid silicate was almost complete, with only a low concentration of small sulfide droplets (Φ <90
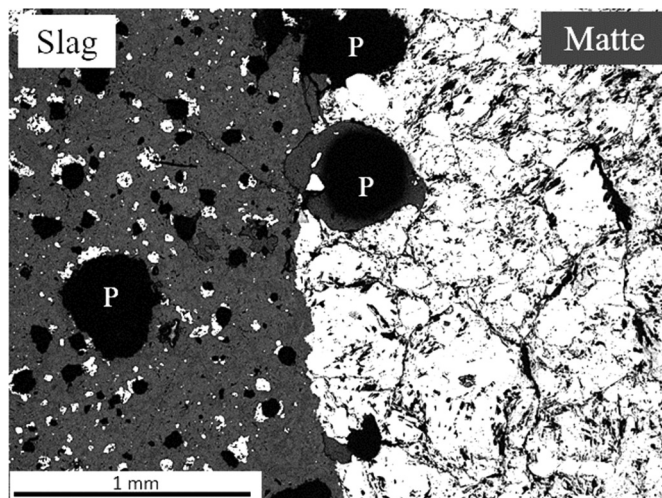

Figure 13. Optical micrograph of platreef concentrate fired at 1400°C, showing the collection of a matte button at the bottom of the crucible (P: pore).

μm) remaining in the slag, even though the gangue components did not exhibit complete melting.

Only after heating UG–2 concentrate at 1480°C was the concentration of the liquid silicate phase sufficient to allow the matte prills to settle and collect at the bottom of the crucible. The matte button consisted of sulfides, PGM-containing alloys and faceted $FeCr_2O_4$ spinel crystals at the matte boundary (Figure 14). The Ni:Fe atomic ratio of the alloy varies between 1.26:1 and 0.87:1, while the bright areas are primarily composed of iron and nickel, but also contains
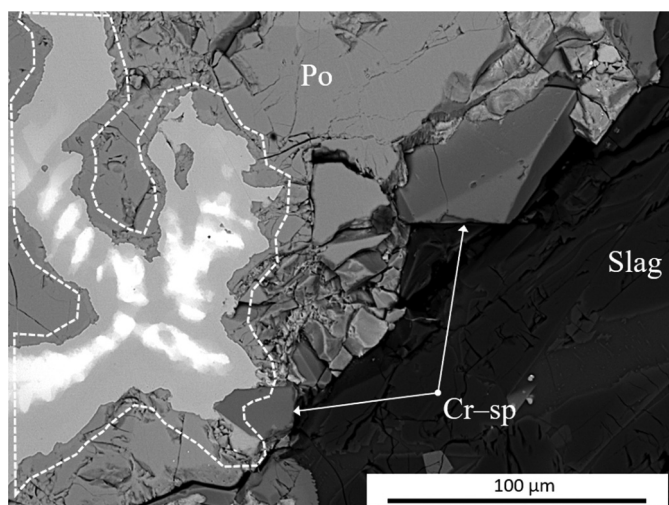
Figure 14. BEI of UG–2 concentrate heated at 1480°C, showing a matte-forming assemblage at the bottom of the crucible (Po: pyrrhotite; Cr – sp: $FeCr_2O_4$ spinel; PGM-containing alloy marked by a dashed line).

copper, cobalt and PGMs (54.3–55.4 atomic % Fe; 29.9–38.8 atomic % Ni; ~1.3 atomic % Cu; ~1.6 atomic % Co; max 9.2 atomic % Pt; max 1.8 atomic % Ru; max 0.8 atomic % Rh; max 0.6 atomic % Ir and max 0.2 atomic % Pa). The PGM-containing alloy is hosted in a pyrrhotite substrate with a stoichiometry of $Fe_{0.94}Ni_{0.03}Cu_{0.03}Co_{0.01}S$.

Comparison between slow-cooled (sealed and drilled capsules) and quenched platreef samples (1400 °C). BEI images of the Platreef concentrate fired at 1400°C and slow-cooled (sealed and drilled capsules) versus quenched, are presented in

Table 10. Major crystalline phases found in the mattes (1400°C).

	Matte components (mass %)
Slow cooled, sealed capsule	Pn (72.1%); Tro (21.8%); Po (4.0%); Alloy (2.1%)
Slow cooled, drilled capsule	Pn (78.4%); Tro (21.6%)
Quenched	Pn (48.4%); Tro (38.7%); Po (12.2%); Bn (0.7%)

Pn: pentlandite; Tro: troilite; Po: pyrrhotite; Bn; bornite.

Figure 15(a–c). The microstructures obtained are similar, with matte prills entrained within the LP, matte attachment to pores, and a mixture of enstatite and LP as dominant gangue phases. The quench test, as expected, impacted the microstructures of the gangue phases, exhibiting finer enstatite crystals in the LP matrix compared to the slow-cooled sample (dashed area, Figure 15(c)).

The quantification of the crystalline matte phases in the three tests is presented in Table 10. Bornite in the slow-cooled experiments, as well as dbss and alloy in the drilled experiments, was not detected by XRD. However, the SEM–EDS analyses confirmed the coexistence of these phases as matte-forming assemblages. Slow-cooled samples (both sealed and drilled capsules) exhibited the presence of $FeCr_2O_4$ spinel crystals at the boundaries of the matte droplets, while the quenched test only contained very small crystals (Φ~10 µm), randomly distributed within the matte prills.

Comparison between slow-cooled (sealed and drilled capsules) and quenched platreef samples (1480°C). Porosity observed microstructurally at lower temperatures virtually disappeared at 1480°C. In both the slow-cooled samples (sealed and drilled capsules), matte was pushed to higher positions in the concentrate bed when columnar enstatite crystals crystallized (Figure 16, 1480°C). Conversely, the quenched test exhibited
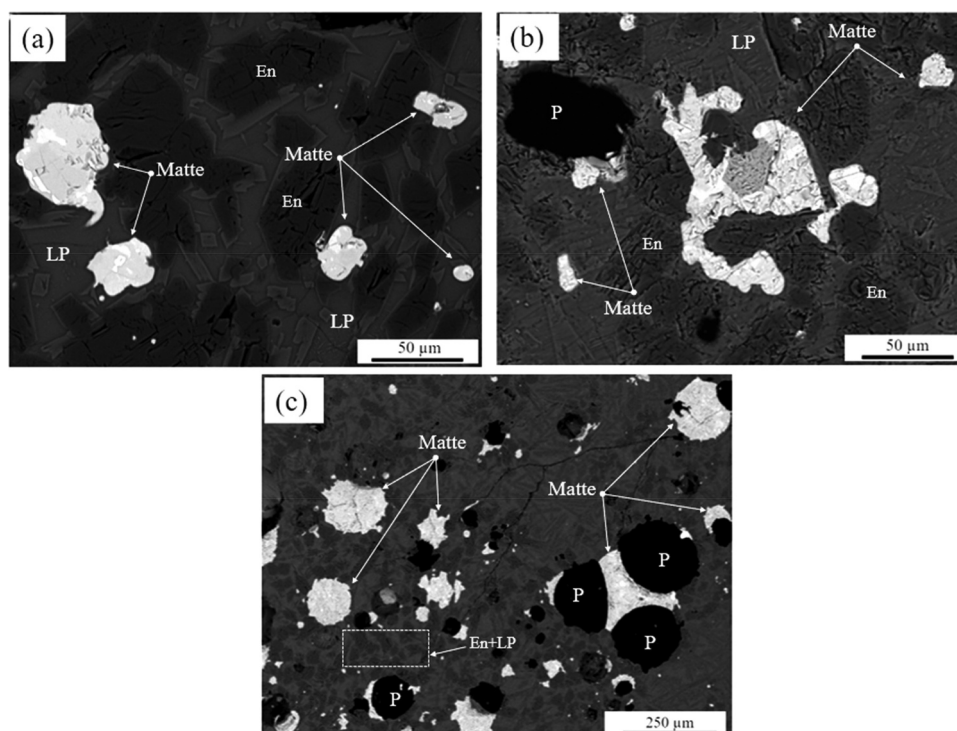

Figure 15. BEI of the platreef concentrate fired at 1400 °C: (a) slow-cooled, sealed capsule (b) slow-cooled, drilled capsule (c) quenched. (En: enstatite; LP: liquid phase; P: pore).
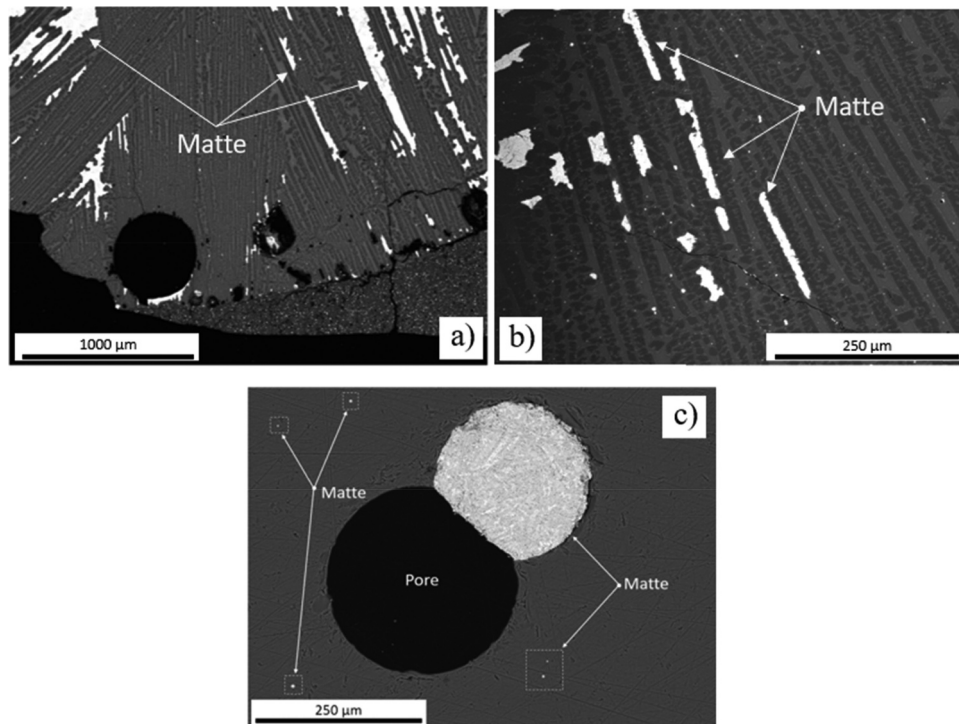
Figure 16. BEI of the platreef concentrate fired at 1480 °C: (a) slow-cooled, sealed capsule (b) slow-cooled, drilled capsule (c) quenched.

Table 11. Major crystalline phases found in the mattes (1480°C).

	Matte components (mass %)
Slow-cooled, sealed capsule	Pn (74.2%); Tro (24.4%); Alloy (1.5%)
Slow-cooled, drilled capsule	Pn (60.00%); Tro (27.8%); Cct (12.2%)
Quenched	Pn (50.38%); Tro (28.93%); Alloy (13.29%); Bn (7.39%); Po (0.01%)

Pn: pentlandite; Tro: troilite; Cct: chalcocite; Bn; bornite; Po: pyrrhotite.

clear signs of complete melting. This sample consisted of a glassy slag with a few matte droplets suspended in the liquid silicate phase, and others attached to some remaining pores (Figure 16(c)).

The matte-forming assemblages observed in the 1480°C tests are similar to those found after firing at 1400°C (compare Tables 10 and 11). Euhedral $FeCr_2O_4$ spinel crystals could be detected again on the boundaries of the matte prills in the slow-cooled samples (sealed and drilled capsule), and small spinel crystals (ϕ~10 µm) were homogeneously dispersed in the quenched matte prills.

Discussion

The temperature gradient across the BT ranges from 800°C at the BT-freeboard interface to 1500°C at the BT-slag interface. At 800°C, the sulfides in the concentrates have already decomposed, while some of them have already melted. The onset of melting of the sulfides (UG-2 concentrate at 640°C and Platreef concentrate at 648°C) was reflected by the spherification of a few nickel sulfide particles in both concentrates after firing at 900°C. As the temperature increased from 900 to 1100°C and higher, the microstructural analysis displays the complete spherification of the matte-forming assemblages, with the exception of some single pyrrhotite crystals, which have the highest melting point of the sulfides (~1196°C). This is consistent with the FactSage predicted liquidus temperatures of 1000°C for the sulfide assemblages of both the Platreef and UG–2 mattes.

At 1200°C, noticeable sintering of the concentrate bed occurred, which is also the temperature at which all sulfide minerals have either decomposed or melted. These molten sulfide droplets are squeezed into the porosity created by the sintered silicate bed, but matte did not segregate from the gangue. With a further increase in temperature to 1300°C, a decrease in the number of sulfide particles in the Platreef concentrate and the simultaneous increase in their average size is associated with the merging, coalescence and settling of sulfide prills through the silicate liquid phase from the gangue. At this temperature (1300°C), partial matte separation takes place in the Platreef concentrate when 52% liquid silicate is present, forming a continuous path along which the sulfide droplets can settle through gravitation. In contrast, the low liquid silicate content of 26% in the UG-2 concentrate is not sufficient to facilitate coalescence, with the consequence that most of the sulfide droplets remain entrained in the porosity associated with the gangue. At 1400°C, the 88.7% liquid silicate phase present facilitates effective matte–gangue separation in the Platreef concentrate, while this does not occur in the UG–2 concentrate when 75% liquid silicate is present. Matte–gangue separation in the UG–2 concentrate takes place at 1480°C

when virtually all the gangue is molten, although a very low concentration of sulfides is present.

PGM collection occurred through the incorporation of PGMs in the Ni–Fe–based solid solution alloy phase, forming PGM-enriched crystals from 900°C up to 1100°C (UG–2 concentrate). In the PGM-bearing sulfides, the majority of PGMs occur in solid solution with pyrrhotite and pentlandite and, to a lesser extent, as Pd antimonides and arsenides in some pyrite, chalcopyrite and millerite (Smith, Holwell, and McDonald 2014). Therefore, the complete melting of the PGM-bearing minerals (after firing at 1200°C and above) promotes the liquid-state diffusion of the PGMs in the liquid matte.

The morphology of the sulfides that crystallized after firing is dominated by exsolution textures, which coarsen with increased cooling times. However, the observed resulting phases do not agree well with the thermochemical FactSage predictions, presumably due to equilibrium not being maintained during cooling. FactSage predicted the presence of two FCC alloys, a nickel-rich and a Cu-rich alloy phase, while only a Ni-rich Ni-Fe alloy phase was found in the cooled mattes. Pentlandite was observed in the majority of cooled matte samples, while this phase was not predicted by FactSage. Ni–Fe solid solution alloy particles, pentlandite, iron sulfides (pyrrhotite and troilite) and dbss were detected as major sulfide phases in the crystallized mattes between 800 and 1300°C. This observation is consistent with the literature, which reports the association of pentlandite [(Fe,Ni)$_9$S$_8$] with dbss – pyrrhotite [(Fe,Ni)$_{1-x}$S] phase assemblages in recrystallized low-temperature Fe-Ni-Cu-S-based mattes (Andrews and den Hoed 2011; Du Toit, Cromarty, and Garbers-Craig 2016; Eksteen 2011; Govender 2006; Zhu et al. 2021). Exsolution of pentlandite from the monosulfide solid solution phase (mss), which exhibits complete solid solution between the FeS and NiS end – members above 610°C, was also reported by Wang (2006). The coexistence of alloy, pentlandite and pyrrhotite is also common in crystallized industrial mattes from PGM nickel industries (Chen et al. 2017; Lamya and Lorenzen 2006; Page 1982; Snyders et al. 2018) and in natural environments (Hudson and Travis 1981; Thyse 2014).

Conclusions

The phase evolution of sulfides in UG–2 and Platreef concentrates, as well as matte drainage, over a temperature range from 800 to 1480°C was examined on a laboratory scale. The following conclusions can be drawn:

- At 800°C, the sulfides in the concentrates have already decomposed, while some of them have already melted.
- When sintering of the concentrate bed commences (1200°C), matte droplets are trapped in the porosity of the bed, but do not separate from the gangue.
- Coalescence of sulfide particles and droplets takes place after the formation of a considerable amount of liquid silicate: 42.7% (1300°C) for partial separation and 73.3% (1400°C) and 82.6% (1480°C) for complete separation in the Platreef concentrate; 99.73% for complete separation in the UG–2 concentrate at 1480°C.

- Matte–gangue separation starts at temperatures above the solidus temperature of the gangue but below its liquidus temperature. The liquid silicate phase that forms acts as a pathway for the matte droplets, enabling them to coalesce and settle through the black top.
- Increased temperatures increase the concentration of the liquid silicate phase and decrease its viscosity, thereby further facilitating the coalescence and collection of matte.
- Higher concentrations of sulfide minerals in the concentrate enhance the probability of matte prills colliding, merging into larger droplets, and separating from the gangue.
- When blending concentrates in a PGM smelter, the solidus temperature of the gangue, the viscosity of the liquid silicate phase that forms, and the total concentration of sulfide minerals in the concentrate will directly impact its effective matte separation.
- At temperatures as low as 900°C, PGMs are already collected in the Ni–Fe-based alloy that forms.

Disclosure statement

No potential conflict of interest was reported by the author(s).

ORCID

Oscar Rivera Li Kao http://orcid.org/0000-0002-6146-9828
Andrie Garbers-Craig http://orcid.org/0000-0002-0298-8097

References

Adams, M., K. Liddell, and T. Holohan. 2011. Hydrometallurgical processing of platreef flotation concentrate. *Minerals Engineering* 24 (6):545–50. doi:10.1016/j.mineng.2010.09.009.

Andrews, A., and P. den Hoed. 2011. Mineralogical solutions for pyrometallurgical problems. In *Southern African pyrometallurgy 2011*, ed. R. T. Jones and P. den Hoed, 199–207. Johannesburg, South Africa: Southern African Institute of Mining and Metallurgy.

Anthony, W., R. Bideaux, K. Bladh, and M. Nichols. 2005. *Handbook of mineralogy*. Chantilly, VA: Mineralogical Society of America.

Bacedoni, M., I. Moreno-Ventas, and G. Ríos. 2020. Copper flash smelting process balance modeling. *Metals* 10 (9):1–19. doi:10.3390/met10091229.

Bale, C. W., E. Bélisle, P. Chartrand, S. A. Decterov, G. Eriksson, A. E. Gheribi, K. Hack, I. H. Jung, Y. B. Kang, J. Melançon, et al. 2016. FactSage thermochemical software and databases, 2010–2016. *Calphad: Computer Coupling of Phase Diagrams and Thermochemistry* 54:35–53. doi:10.1016/j.calphad.2016.05.002.

Ballhaus, C., M. Tredoux, and A. Späth. 2001. Phase relations in the Fe–Ni–Cu–PGE–S system at magmatic temperature and application to

massive sulphide ores of the Sudbury igneous complex. *Journal of Petrology* 42 (10):1911–26. doi:10.1093/petrology/42.10.1911.

Barnes, A. R., and A. F. Newall. 2006. Spinel removal from PGM smelting furnaces. In *Southern African pyrometallurgy 2006*, ed. R. T. Jones, 77–88. Johannesburg, South Africa: South African Institute of Mining and Metallurgy.

Buchspies, B., L. Thormann, C. Mbohwa, and M. Kaltschmitt. 2017. PGE production in Southern Africa, part II: Environmental aspects. *Minerals* 7 (11):225. doi:10.3390/min7110225.

Cawthorn, R. G. 2006. Centenary of the discovery of platinum in the bushveld complex. *Platinum Metals Review* 50 (3):130–33. doi:10.1595/147106706X119746.

Charlier, B., O. Namur, R. Latypov, and C. Tegner.2015. *Layered intrusions*, ed. B. Charlier, O. Namur, R. Latypov, & C. Tegner. Springer Science+Business Media. doi:10.1007/978-94-017-9652-1.

Chen, G. J., J. M. Gao, M. Zhang, and M. Guo. 2017. Efficient and selective recovery of Ni, Cu, and Co from low-nickel matte via a hydrometallurgical process. *International Journal of Minerals, Metallurgy and Materials* 24 (3):249–56. doi:10.1007/s12613-017-1402-9.

Cramer, L. A. 2001. The extractive metallurgy of South Africa's platinum ores. *JOM* 53 (10):14–18. doi:10.1007/s11837-001-0048-1.

Crundwell, F. (F. K. Crundwell, M. S. Moats, V. Ramachandran, T. G. Robinson. 2011. *Extractive metallurgy of nickel and cobalt*, ed. W. G. Davenport. Elsevier Ltd. https://www.sciencedirect.com/book/9780080968094/extractive-metallurgy-of-nickel-cobalt-and-platinum-group-metals.

Du Toit, J., R. D. Cromarty, and A. M. Garbers-Craig. 2016. Matte– taphole clay – refractory brick interaction in a PGM smelter. *The Journal of the Southern African Institute of Mining and Metallurgy* 116 (4):339–42. doi:10.17159/2411-9717/2016/v116n4a6.

Eksteen, J. J. 2011. A mechanistic model to predict matte temperatures during the smelting of UG2-rich blends of platinum group metal concentrates. *Minerals Engineering* 24 (7):676–87. doi:10.1016/j.mineng.2010.10.017.

Eksteen, J. J., B. Van Beek, and G. A. Bezuidenhout. 2011. Cracking a hard nut: An overview of Lonmin's operations directed at smelting of UG2-rich concentrate blends. *Journal of the Southern African Institute of Mining and Metallurgy* 111 (10):681–90.

Engelbrecht, J. U. 2012. Potential changes in the physical beneficiation processes that can improve the recovery grade or costs for the platinum group metals. In *Proceedings of the Fifth International Platinum Conference: A Catalyst for Change*, Sun City, South Africa, September 17–21, 2012, 343–59. Southern African Institute of Mining And Metallurgy.

Fagerlund, K. O., and H. Jalkanen. 2001. Microscale simulation of settler processes in copper matte smelting. *Metallurgical and Materials Transactions B: Process Metallurgy and Materials Processing Science* 32 (3):555–57. doi:10.1007/s11663-001-0040-8.

Gaballah, I., E. Allain, M.-C. Meter-Joly, and K. Malau. 1994. Thermal treatment of complex sulfide ores in N_2 and H_2 atmospheres: A new approach for the extraction of their valuable elements. *Metallurgical and Materials Transactions B: Process Metallurgy and Materials Processing Science* 25 (2):193–205. doi:10.1007/BF02665202.

Govender, S. 2006. Micro PIXE analyses of furnace and converter mattes for the determination of trace element distribution and concentrations. MSc thesis, University of Zululand.

Guntoro, P. I., A. Jokilaakso, N. Hellstén, and P. Taskinen. 2018. Copper matte - slag reaction sequences and separation processes in matte smelting. *Journal of Mining and Metallurgy, Section B: Metallurgy* 54 (3):301–11. doi:10.2298/JMMB180214021G.

Gwimbi, P. 2017. Monitoring SO_2 emission trends and residents' perceived health risks from PGM smelting at Selous metallurgical complex in Zimbabwe. *International Journal for Equity in Health* 16 (1):1–11. doi:10.1186/s12939-017-0696-6.

Hudson, D. R., and G. A. Travis. 1981. A native nickel-Heazlewoodite-ferroan trevorite assemblage from Mount Clifford, Western Australia. *Economic Geology* 76 (6):1686–97. doi:10.2113/gsecongeo.76.6.1686.

Jones, R. T. 2004. JOM world nonferrous smelter survey, part II: Platinum group metals. *JOM* 56 (12):59–63. doi:10.1007/s11837-004-0238-8.

Jones, R. T. 2005. An overview of South African PGM smelting, Nickel and Cobalt 2005: Challenges in extraction and production. In *44th Annual Conference of Metallurgists*, Calgary, Canada, August 21–24, 147–78. CIM (Canadian Institue of Mining, Metallurgy and Petroleum).

Jones, R. T., and I. J. Kotzé. 2004. DC arc smelting of difficult PGM-containing feed materials. In *International Platinum Conference 'Platinum Adding Value'*, Sun City, South Africa, 33–36. The Southern African Institute of Mining and Metallurgy.

Kullerud, G. 1963. Thermal stability of pentlandite. *The Canadian Mineralogist* 7 (3):353–66.

Lamya, R. M., and L. Lorenzen. 2006. Atmospheric acid leaching of nickel- copper matte froM impala platinum refineries. *The Journal of the South African Institute of Mining and Metallurgy* 106:385–96.

Liddell, K. 2009. *25 Years of UG2 concentrators… Mintek 75 - a celebration of technology conference*. Randburg, South Africa: Southern African Institute of Mining and Metallurgy.

Mabiza, L. 2006. An overview of PGM smelting in zimbabwe - zimplats operations. In *Southern African pyrometallurgy 2006*, ed. R. T. Jones, 63–75. Johannesburg, South Africa: South African Institute of Mining and Metallurgy.

Madelung, O., U. Rössler, and M. Schulz, Eds. 2000. *Chalcopyrite ($CuFeS_2$) crystal structure, lattice parameters, density, melting point: Datasheet from Landolt-Börnstein - group III condensed matter · volume 41e: "ternary compounds, organic semiconductors", springermaterials*. Berlin Heidelberg: Springer-Verlag. doi:10.1007/10717201_225.

Mberi, T., L. L. Mguni, and F. Ntuli. 2018. Effect of frother and depressant interaction on flotation of great Dyke PGM ore. *Journal of the Southern African Institute of Mining and Metallurgy* 118 (1):65–69. doi:10.17159/2411-9717/2018/v118n1a8.

McLaren, C. H., and J. P. R. De Villiers. 1982. The platinum-group chemistry and mineralogy of the UG-2 chromitite layer of the bushveld complex. *Economic Geology* 77 (6):1348–66. doi:10.2113/gsecongeo.77.6.1348.

Mineralogical Society of America. 1974. *Short course notes, sulfide mineralogy*. Mineralogical Society of America. http://www.minsocam.org/msa/collectors_corner/arc/scn1.htm.

Muzawazi, C., and J. Petersen. 2015. Heap and tank leaching of copper and nickel from a platreef flotation concentrate using ammoniacal solutions. *Canadian Metallurgical Quarterly* 54 (3):297–304. doi:10.1179/1879139515y.0000000017.

Mwase, J. M., J. Petersen, and J. J. Eksteen. 2012. Assessing a two-stage heap leaching process for platreef flotation concentrate. *Hydrometallurgy* 129–130:74–81. doi:10.1016/j.hydromet.2012.09.007.

Nell, J. 2004. Melting of platinum group metal concentrates in South Africa. *Journal of the South African Institute of Mining and Metallurgy* 104 (7):423–28.

Nelson, L. R., G. A. Georgalli, K. L. Hines, and R. J. Hundermark. 2018. Converter processing of platinum group metals. *Mineral Processing & Extractive Metallurgy* 128 (1–2):134–59. doi:10.1080/25726641.2018.1506272.

Nieroda, P., J. Leszczyński, A. Mikuła, K. Mars, M. J. Kruszewski, and A. Koleżyński. 2020. Thermoelectric properties of Cu_2S obtained by high temperature synthesis and sintered by IHP method. *Ceramics International* 46 (16):25460–66. doi:10.1016/j.ceramint.2020.07.016.

O'Connor, C., and T. Alexandrova. 2021. The geological occurrence, mineralogy and processing by flotation of platinum group minerals (PGMs) in South Africa and Russia. *Minerals* 11 (1):54. doi:10.3390/min11010054.

Oberthür, T. 2011. Platinum-group element mineralization of the main sulfide zone, Great Dyke, Zimbabwe. Reviews in economic geology magmatic Ni-Cu and PGE deposits: Geology, geochemistry, and genesis, ed. Li, C. and Ripley, E.M. *Society of Economic Geologists* 17:329–49. doi:10.5382/Rev.17.12.

Oberthür, T., T. W. Weiser, and K. Kojonen. 2002. Local variations and regional trends in PGE geochemistry and mineralogy in the main sulfide zone of the great Dyke, Zimbabwe. https://www.researchgate.net/publication/237570915.

Page, M. L. 1982. A mineralogical study of nickel mattes from the Kalgoorlie nickel smelter, Kalgoorlie, Western Australia. *Metallurgical Transactions B* 13B (June):141–52. doi:10.1007/BF02664571.

Prasad, S., and B. D. Pandey. 1999. Thermoanalytical studies on copper-iron sulphides. *Journal of Thermal Analysis and Calorimetry* 58 (3):625–37. doi:10.1023/A:1010108729034.

Ramonotsi, M. 2011. Characterisation of the effect of alteration on the PPM platinum ore and evaluation of selected strategies to improve metallurgical performance. MSc thesis, University of Cape Town.

Rivera Li Kao, O., and A. Garbers-Craig. 2022. Impact of phase evolution in platreef and UG-2 concentrates on matte drainage in the black top of a platinum group metal smelter. *Mineral Processing and Extractive Metallurgy Review* 43 (3):326–38. doi:10.1080/08827508.2020.1861613.

Schindelin, J., I. Arganda-Carreras, E. Frise, V. Kaynig, M. Longair, T. Pietzsch, S. Preibisch, C. Rueden, S. Saalfeld, B. Schmid, et al. 2012. Fiji: An open-source platform for biological-image analysis. *Nature Methods* 9 (7):676–82. doi:10.1038/nmeth.2019.

Schouwstra, R. P., E. D. Kinloch, and C. A. Lee. 2000. A short geological review of the bushveld complex. *Platinum Metals Review* 44 (1):33–39. doi:10.1595/003214000X4413339.

Shaw, A., L. P. V. S. De Villiers, R. J. Hundermark, J. Ndlovu, L. R. Nelson, B. Pieterse, R. Sullivan, N. Voermann, C. Walker, F. Stober, et al. 2013. Challenges and solutions in PGM furnace operation: High matte temperature and copper cooler corrosion. *Journal of the Southern African Institute of Mining and Metallurgy* 113 (3):251–61.

Smith, J. W., D. A. Holwell, and I. McDonald. 2014. Precious and base metal geochemistry and mineralogy of the grasvally norite–pyroxenite–anorthosite (GNPA) member, northern bushveld complex, South Africa: Implications for a multistage emplacement. *Mineralium Deposita* 49 (6):667–92. doi:10.1007/s00126-014-0515-6.

Snyders, C. A., G. Akdogan, G. Thompson, S. M. Bradshaw, and A. P. Van Wyk. 2018. Investigating the behaviour of PGEs during first-stage leaching of a Ni-Fe- Cu-S converter matte. *The Journal of the Southern African Institute of Mining and Metallurgy* 118:353–60. doi:10.17159/2411-9717/2018/v118n4a4.

Stribrny, B., F. W. Wellmer, K. P. Burgath, T. Oberthür, M. Tarkian, and T. Pfeiffer. 2000. Unconventional PGE occurrences and PGE mineralization in the Great Dyke: Metallogenic and economic aspects. *Mineralium Deposita* 35 (2–3):260–80. doi:10.1007/s001260050019.

Sugaki, A., and A. Kitakaze. 1998. High form of pentlandite and its thermal stability. *American Mineralogist* 83 (1–2):133–40. doi:10.2138/am-1998-1-213.

Thyse, E. L. 2014. Effect of iron endpoint during Peirce-Smith converting on matte mineralogy and downstream processing of base and platinum- group metals. PhD diss., University of Stellenbosch.

Ulbrich, K. F., and C. E. M. Campos. 2020. Nanocrystalline Ni_3S_2 prepared by mechanochemistry and its behavior at high temperatures and high pressure. *Journal of Magnetism and Magnetic Materials* 493:165706. doi:10.1016/j.jmmm.2019.165706.

Vermaak, M. K. G. 2005. Fundamentals of the flotation behaviour of palladium bismuth tellurides. PhD thesis, University of Pretoria.

Waldner, P., and A. D. Pelton. 2005. Thermodynamic modelling of the Fe-S system. *Journal of Phase Equilibria & Diffusion* 26 (1):23–38. doi:10.1361/15477030522455.

Wang, H. 2006. Isothermal kinetics of the pentlandite exsolution from mss/pyrrhotite using model-free method. *Tsinghua Science and Technology* 11 (3):368–73. doi:10.1016/S1007-0214(06)70202-4.

Wilson, M. G. C., and C. R. Anhaeusser. 1998. *The mineral resources of South Africa*, 6th ed. Silverton, South Africa: Council of Geoscience.

Xu, H., X. Guo, L. A. Seaman, A. J. Harrison, S. J. Obrey, and K. Page. 2019. Thermal desulfurization of pyrite: An in situ high-T neutron diffraction and DTA-TGA study. *Journal of Materials Research* 34 (19):3243–53. doi:10.1557/jmr.2019.185.

Zhu, C., Y. Lei, X. Hu, Q. Xu, X. Zou, H. Cheng, and X. Lu. 2021. Effective removal of barrier layer on the surface of low-nickel matte in an $FeCl_3$-HCl-H_2O solution. *Minerals* 11 (11):1219. doi:10.3390/min11111219.